Princeton Plasma Physics Laboratory

PPPL- 5111

PPPL-5111

The Contribution of RF Rectification to Field-Aligned Losses of HHFW Power to the Divertor in NSTX

R.J. Perkins, J.C. Hosea, M.A. Jaworski,
J-W. Ahn, A. Diallo, *et al.*

January 2015

Prepared for the U.S. Department of Energy under Contract DE-AC02-09CH11466.

Princeton Plasma Physics Laboratory
Report Disclaimers

Full Legal Disclaimer

Trademark Disclaimer

PPPL Report Availability

Princeton Plasma Physics Laboratory:

http://www.pppl.gov/techreports.cfm

Office of Scientific and Technical Information (OSTI):

http://www.osti.gov/scitech/

Related Links:

U.S. Department of Energy

Office of Scientific and Technical Information

The Contribution of RF Rectification to Field-Aligned Losses of HHFW Power to the Divertor in NSTX

R J Perkins[1], J C Hosea[1], M A Jaworski[1], J-W Ahn[2], A Diallo[1], R E Bell[1], N Bertelli[1], S Gerhardt[1], T K Gray[2], G J Kramer[1], B P LeBlanc[1], A McLean[3], C K Phillips[1], M Podestà[1], L Roquemore[1], S Sabbagh[4], G Taylor[1] and J R Wilson[1]

[1]Princeton Plasma Physics Laboratory, Princeton, NJ

[2]Oak Ridge National Laboratory, Oak Ridge, TN

[3]Lawrence Livermore National Laboratory, Livermore, CA

[4]Columbia University, New York, NY

E-mail: rperkins@pppl.gov

Abstract. NSTX can exhibit a major loss of high-harmonic fast wave (HHFW) power to the upper and lower divertor regions along scrape-off layer (SOL) field lines passing in front of the antenna, resulting in bright and hot spirals on both the upper and lower divertor regions. One possible mechanism for this loss is RF sheaths forming at the divertors. Here we demonstrate that swept-voltage Langmuir probe characteristics for probes under the spiral are shifted relative to those not under the spiral in a manner consistent with RF rectification. We estimate both the magnitude of the RF voltage across the sheath and the sheath heat flux transmission coefficient in the presence of the RF field. Although precise comparison between the computed heat flux and infrared (IR) thermography cannot yet be made, the computed heat deposition compares favorably with the projections from IR camera measurements. The RF sheath losses are significant and contribute substantially to the total SOL losses of HHFW power to the divertor for the cases studied. This work will guide future experimentation on NSTX-U, where a wide-angle IR camera and a dedicated set of coaxial Langmuir probes for measuring the RF sheath voltage directly will quantify the contribution of RF sheath rectification to the heat deposition from the SOL to the divertor.

PACS: 52.50.Qt, 52.35.-g, 52.55.Fa, 52.70.Gw

1. Introduction

Plasma heating using waves in the ion-cyclotron range of frequencies (ICRF) is an important technique for tokamaks, and up to 20 MW of ICRF power is planned for ITER [1]. With respect to the spherical-tokamak geometry, high-harmonic fast-wave heating (HHFW) [2] is envisioned to aid in plasma start-up to help obtain complete non-inductive operation [3]. There are several issues in both scrape off layer (SOL) and core-plasma physics for which it is important to know how much fast-wave power is coupled to the core plasma and how much is lost to the SOL; these physics issues include modeling plasma start-up, fast-wave absorption by fast ions [4-6], and the RF losses to the divertor plates via the SOL.

One outstanding issue regarding HHFW heating experiments on the National Spherical Torus eXperiment (NSTX) [7] is a significant power loss that can occur directly in the SOL [8], producing bright and hot spirals on both the upper and lower divertor regions [9-11], as shown in Fig. 1. For shot 130621, only approximately 40% of the RF power coupled from the antenna reaches the core plasma, while an infrared (IR) camera [12] measures an RF-produced heat flux within the spiral of up to ~ 2 MW/m^2 [9] (k_ϕ = -8 m^{-1} or -90° phasing between antenna straps,

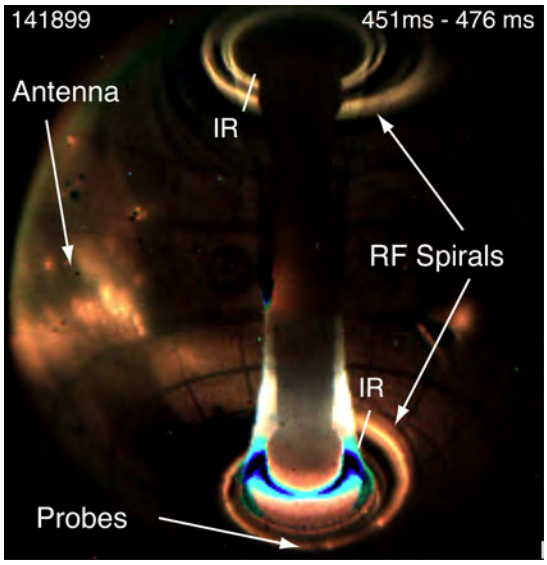

Figure 1. RF spirals produced on the bottom and top divertor plates of NSTX with HHFW heating. IR measurement locations are at Bay I bottom and Bay G top as indicated. Four swept-voltage Langmuir probes are located at Bay B just outboard of the vessel gap. Plasma conditions are B_T = 4.5 kG, I_p = 1.0 MA (magnetic pitch in the SOL ~ 39.6°), P_{RF} = 1.3 MW, P_{NB} = 2 MW, and deuterium.

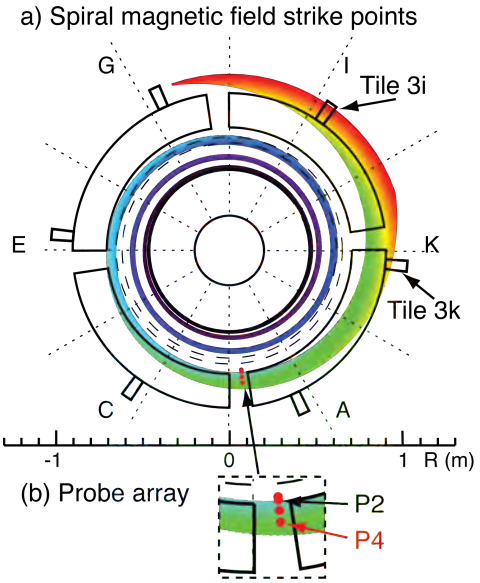

Figure 2. (a) Calculated spiral location on the bottom divertor using the SPIRAL code for field lines passing in front of the HHFW antenna in the SOL. Color signifies the radial location of the field line at the midplane: red is near the antenna and black is near the LCFS. Conditions of Fig. 1, shot 141899 at 433 ms. (b) Expanded view of four probes at Bay B. Probe R (cm) values 1 – 4: 63.82, 64.67, 67.49, and 70.59.

and P_{RF} = 1.8 MW/m^2), although the peak observed heat flux is typically smaller. The heating efficiency of the HHFW system is a strong function of the magnetic field strength, the toroidal wavenumber k_ϕ, and the edge density [8-11], suggesting that the SOL losses are intimately connected with the location of the righthand cutoff, a hypothesis that is being observed in full-wave simulations [13]. Importantly, these spirals have been shown to be the footprints of SOL field lines that pass directly in front of the antenna [14], as has been determined by field-line mapping using the SPIRAL code [15], as shown in Fig. 2a for shot 141899. This includes all SOL field lines passing in front of the antenna between the antenna and the last closed flux surface (LCFS), and not just those lines connected to antenna components. Other diagnostics for investigating the RF heat deposition on the divertor include both a four-element radial array of swept-voltage Langmuir probes in the lower divertor region [16, 17], and divertor tiles that have been instrumented to measure currents [18]. The locations of these diagnostics relative to the RF spiral are shown in Figs. 1 and 2b.

This paper demonstrates, for selected discharges with both RF and neutral beam (NB) power and with only RF power, that RF rectified sheaths are playing an important role in this SOL loss of fast-wave power to the divertor. RF rectification, reviewed in Section 3, occurs when an oscillating RF electric field develops across the sheath at the wall or probe, and results in an enhanced DC electron current at a given bias voltage [19, 20]. RF rectification is often studied in the vicinity of the antenna structure as a possible explanation for impurity injection during ICRF operation [21-23] and to explain RF-induced heat fluxes and hot spots on the antenna structure [24, 25]. In this work, we consider specifically the effect of RF rectification on producing the RF heat deposition on the divertor plates in NSTX, a case that is sometimes referred to as a far-field sheath [26]. Far-field RF sheaths have been

cited as a source of multi-pass damping for regimes where the wave energy is poorly absorbed in the core plasma and circulates through the torus, with a small percentage of the RF power being lost through interacting with the wall via the sheath [27]. Because NSTX produces high-beta plasma with strong single pass absorption in the HHFW regime, the RF spirals and associated losses are direct effects and occur for waves propagating through the SOL away from the antenna but before they cross the last closed flux surface [8, 10]

This paper is structured as follows. In Section 2, we present the probe characteristics for shot 141899 with both HHFW and NB power. Despite SOL turbulence, effects consistent with RF rectification are observed in the characteristics. In Section 3, the fundamental equations of RF rectification are reviewed, and a formula for the heat flux across a sheath in the presence of an RF electric field is derived. These equations are then applied to NSTX data from Section 2, demonstrating a consistent picture in which RF rectification is playing a substantial role in the RF losses under the heat spiral. In Section 4, we show the RF effects on the probe characteristics for a shot with HHFW power alone for which turbulence effects on the probe signals are reduced and for which the RF rectification effects are more clearly observed. Section 5 contains discussion of the results and the steps to be taken on NSTX-U to permit more quantitative evaluations of the RF rectification contribution to the SOL losses.

2. Probe characteristics for the case with both HHFW and NB power

Shot 141899, with 1.3 MW of applied HHFW power and 2 MW of NB power, provides a good opportunity to study the influence of the applied RF power on the Langmuir probes, as the magnetic field for this shot places the heat spiral over the outermost probe of the array (probe 4, P4) but not over probe 2 (P2) just 6 cm inboard. This claim is substantiated by the strong effect of the applied RF on the floating potential of probe 4, V_{flP4}, and the relatively small effect on the floating potential of probe 2, V_{flP2} (Fig. 3); also, the computed location at 433 ms (Fig 2) lies squarely over P4 but not P2 [14]. This shows that the RF losses to the divertor via the SOL are confined primarily to the spiral, which permits comparison of probe characteristics both with and without RF under nearly identical plasma conditions.

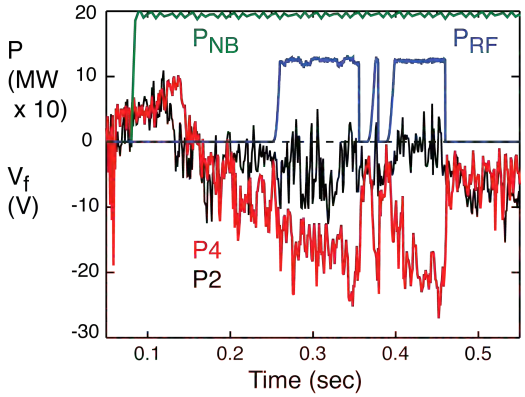

Figure 3. Floating potentials for probes 2 and 4 for shot 141899 (from Ref. 14). Spiral lies over probe 4 (P4) but not probe 2 (P2).

The primary effects of RF rectification are 1) to drive an enhanced electron current to the surface and, 2) for surfaces which are floating (e.g. draw no net current), to drive the floating potential more negative to offset the enhanced electron current [19]. The fast negative response of the floating potential V_{flP4} to the applied RF power is thus consistent with RF rectification, as are the currents to the probes at ground potential ($V_{pr} = 0$): the electron current to probe 4 is enhanced while probe 2 is little effected. This is shown in Fig. 4a, where the current to the probe is plotted for probe bias voltages close to 0 V, (between -0.5 V and + 0.5 V, potentials relative to vessel potential). This response to the RF is very similar to that found on the tile currents with the electron current being enhanced for the tile under the spiral (tile 3i of Fig. 4b) but not from tiles away from the spiral (tile 3k of Fig. 4b).

To further investigate the role of RF rectification, the probe IV characteristics for probes 2 and 4 taken with 1 ms voltage sweeps starting at t = 0.4515 sec are shown in Fig. 5. It is immediately clear that, for the same bias voltage, probe 4 draws more electron current than probe 2, and its floating potential (the intersection of the IV characteristic with the I=0 axis) has shifted to a more negative value. These observations are consistent with RF rectification but could also result from plasma heating, and the large fluctuations in probe current due to the turbulent conditions in the periphery of the discharge make it difficult to discern the underlying cause. For probe 2, an experimental fit is made in the vicinity of the floating potential with I_{sat}, V_{fl}, and T_e of 6 mA, 0 V, and 13 eV. For probe 4, two choices for the exponentials are shown. The first fit is for 10 mA, -30 V, 15 eV with a saturation effect for $V_{pr} > 18$ V; this saturation effect is well known for magnetized plasmas [19]. The large change in floating potential with little change in electron temperature is suggestive of RF rectification. The second fit has 60 mA, -25 V, 31 eV, indicative of plasma heating. It is difficult to choose the proper exponentials for this single sweep case. In order to average over the turbulence, multiple 1 ms consecutive voltage sweeps beginning at t = 0.4515 sec are averaged together giving the characteristics shown in Fig. 6. With a reduced fluctuation level, exponentials with the same ion saturation current and electron temperature but different floating potentials give relatively good fits for both probe characteristics in the vicinity of the floating potential for both probes. This is as expected for RF

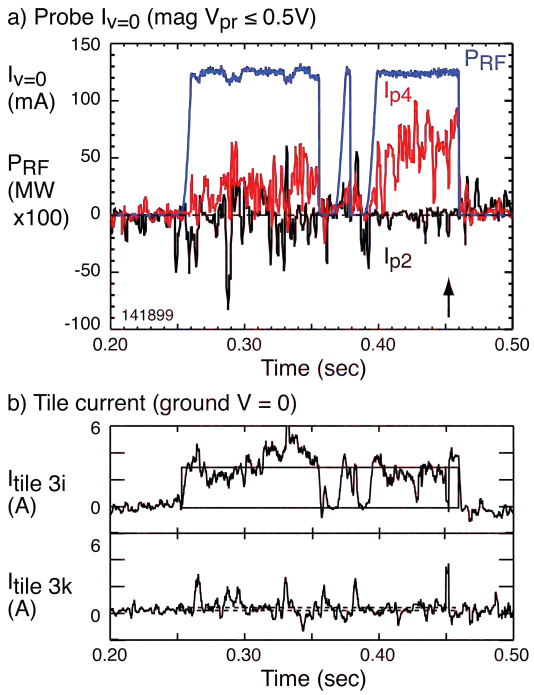

Figure 4. (a) I_{pr} for probes 4 and 2 at V_{pr} = 0 (vessel potential) and (b) tile 3i and 3k currents. The probe and tile under the spiral show significant current away from them (electron current collection).

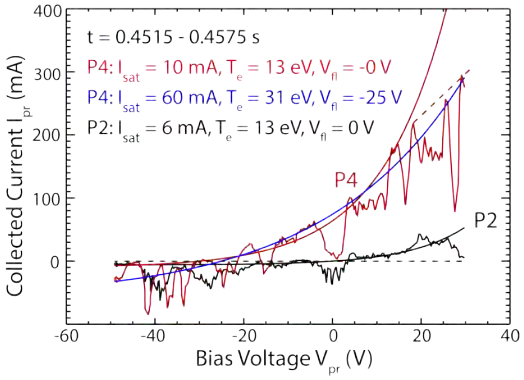

Figure 5. IV characteristics for probes 2 and 4 at 0.4515 sec (arrow in Fig. 3a). Turbulence at divertor plate makes it difficult to choose the red exponential fit (RF rectification) or the blue exponential fit (plasma heating) for P_4 (underneath spiral).

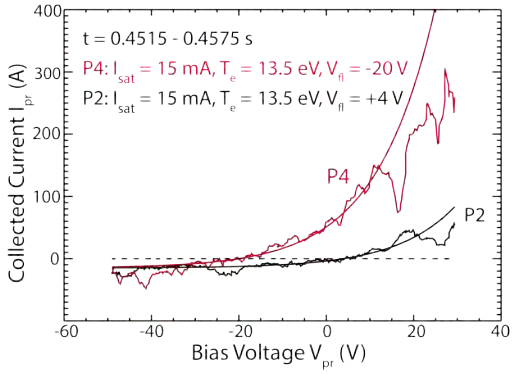

Figure 6. IV characteristics for probes 2 and 4 averaged over 6 consecutive voltage sweeps starting at 0.4515 sec. Exponential fits for probes 2 and 4 have the same I_{sat} and T_e, but different V_{fl} values, indicative of RF rectification.

rectification for which only the floating potential is affected [19] in the exponential ranges of the characteristics.

The temperature that best fits the probe characteristics in Fig. 6, T_e = 13.5 eV, compares well with Thomson scattering measurements at the SOL mid-plane. In Fig. 7, the temperature obtained from the IV characteritics, T_{eIV}, is compared to two temperature profiles measured with Thomson scattering at the two times prior to the end of the RF pulse. The probe midplane positions (major radii) are defined by the field lines connecting the probes to the midplane. It is clear that T_{eIV} = 13.5 eV is in reasonable agreement with the Thomson scattering temperatures at these midplane probe locations. Also plotted is T_e = 31 eV, the hotter electron temperature that fit the probe 4 characteristic reasonably well in Fig. 5 (blue exponential). This hotter electron temperature compares far less favourably with the Thomson scattering data, which furthers the case for RF rectification. It should be noted that the Thomson scattering data is obtained at Bay F outside the field line bundle linking the spiral.

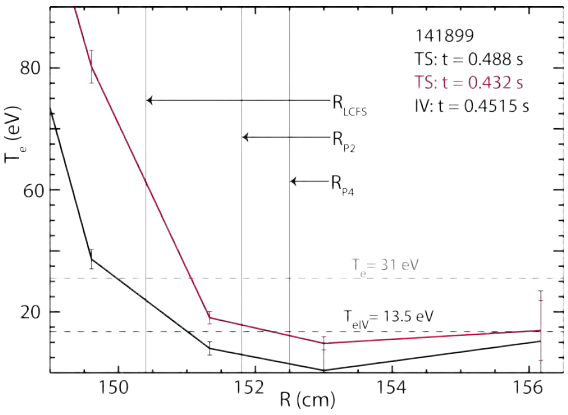

Figure 7. The electron temperature determined from the probe characteristics (T_e =13.5 eV, Fig. 6) is in reasonably good agreement with Thomson scattering measurements at the midplane. Probes 2 and 4 map along field lines to R = 151.8 cm and 152.5 cm at the midplane, and the LCFS midplane radius is 150.4 cm.

3. RF rectification and RF heat flux transmission at a sheath

This section reviews the fundamental equations for Langmuir probes and RF rectification. The average sheath heat flux transmission factor in the presence of an RF field is derived and is shown to be substantially greater than the transmission factor with no RF. The equations presented here are used to estimate the amplitude of the RF voltage and the heat deposition due to RF fields onto the divertor region of NSTX.

3.1 RF rectification

For a Maxwellian electron distribution function, the IV characteristic of a Langmuir probe biased below the plasma potential exhibits exponential behaviour for sufficiently negative bias voltage so that the magnetic field is not affecting the electron current to the probe [28]. In the exponential region:

$$I(V) = I_{sat}\left(-1 + \exp\left((V - V_{flpl})/T_e\right)\right), \quad 1)$$

where V is the probe bias, I_{sat} is the ion saturation current, V_{flpl} is the floating potential relative to plasma potential (as opposed to the vessel potential), and T_e (eV) ≡ kT_e (°K)/e here. V_{flpl} is given by [29, Eq. 25.31]

$$V_{flpl} = \frac{1}{2}\ln\left(2\pi\frac{m_i}{m_e}\left(1+\frac{T_i}{T_e}\right)\right), \quad 2)$$

with δ_e being the secondary electron emission coefficient. It is the non-linear nature of this IV characteristic that gives rise to RF rectified effects; upon adding a sinusoidal potential to the probe bias, the probe will drawn more electron current on the positive excursion of this oscillating potential than it will on the negative excursion. If the probe potential always remains in the range over which the IV characteristic exhibits exponential behaviour and the sheath thickness does not vary significantly with RF potential, then the average current can be computed using the relation [30, Eq. 9.6.16]

$$I_0(x) = \frac{1}{2\pi}\int_0^{2\pi} \exp(x\sin\theta)\,d\theta, \qquad 3)$$

with I_0 being the modified Bessel function of order zero. Expressing V as the sum of a bias voltage and a sinusoidal potential, e.g. V -> V + V_{RF} sin(ωt), and averaging over an RF cycle, the average current drawn by the probe is

$$I_{pr}^{ave}(V) = I_{sat}\left[-1 + I_0\left(\exp((V-V_{flpl})/T_e)\right)\right]. \qquad 4)$$

Since $I_0(x) > 1$ for all x, the electron current drawn by the probe is enhanced for a given probe bias, as is observed on the current-measuring tile 3i in Fig. 4b and on probe 4 in Fig. 4a and Fig. 6. The floating potential with RF, V_{flRF}, is the probe bias voltage at which no net current is drawn by the probe: $I_{pr}^{ave} = 0$ in Eq. 4 [19]:

$$\exp((V_{flRF}-V_{flpl})/T_e) = I_0(V_{RF}/T_e), \qquad 5)$$

where V_{flpl} remains the floating potential in the absence of V_{RF}.

We can now apply Eq. 5 to get an estimate of the RF voltage at the sheath for probe 4. In Fig. 6, $V_{flpl} - V_{flRF} = V_{flP2} - V_{flP4} = 4$ V + 20 V = 24 V. Then, with $T_e = 13.5$ V, the value of V_{RF} is 43.7 V.

3.2 Average RF heat flux transmission

We can similarly quantify the average of the heat flux through a sheath to a surface in the presence of an RF field. The heat flux to a surface is:

$$q = \gamma n_e c_s T_e, \qquad 6)$$

where γ is the sheath transmission factor. γ has been computed from first-principles [29, Eq. 25.54] in the absence of RF fields to be

$$\gamma(V) = \exp(-V/T_e + 2.5)\left[\delta_e + 2\sqrt{2\pi m_e/m_i}\left(1+\delta_e\right)\right]. \qquad 7)$$

Again, the voltages in Eq. 7 are defined relative to plasma potential, but the probe measurements are relative to the vessel potential. To express Eq. 7 in voltages measured by the probe, define $V = V_{flpl} + \Delta V$, so that Eq. 7 can be rewritten using Eq. 2 to give

$$\gamma(V) = \exp(-V_{flpl}/T_e - \Delta V/T_e + 2.5)\left[\delta_e + 2\sqrt{2\pi m_e/m_i}\left(1-\delta_e\right)\exp(\Delta V/T_e)\right]. \qquad 8)$$

The heat flux to the probe at vessel potential, $V_{pr} = 0$, is also the heat flux delivered to the surrounding divertor tiles. Let V_{fl0} denote the floating potential relative to the vessel potential without RF; then at ground potential $\Delta V = - V_{fl0}$. This gives

$$\gamma = -\frac{V_{fl0}}{2.5\, T_e + 21 - V_{fl0}}. \qquad 9)$$

With RF applied, we add an oscillating potential, $\Delta V = - V_{fl0} + V_{RF} \sin(\omega t)$, and average γ over an RF cycle as in Eq. 3 to give

$$\gamma = -\frac{V_{fl0}}{2.5\, T_e + 21 - \frac{V_{fl0}}{\sqrt{2}}} \qquad 10)$$

Using Eq. 5 from above with the floating potentials relative to ground, $V_{flRF} \rightarrow V_{flRF0}$ and $V_{fl} \rightarrow V_{fl0,}$

$$\gamma = -\frac{V_{fl0}}{2.5\, T_e + 21 - V_{fl0}}. \qquad 11)$$

This equation can give a substantial increase in γ and hence in the incident heat flux with an RF field added.

It should be noted that these equations only apply if the probe voltage (bias plus RF) remains in the range in which the IV characteristic without RF is exponential. For un-magnetized plasma, the IV characteristic can remain exponential up to the plasma potential, but for magnetized plasma intercepting a material surface at an oblique angle, deviation from exponential behaviour will occur at lower probe voltages [28].

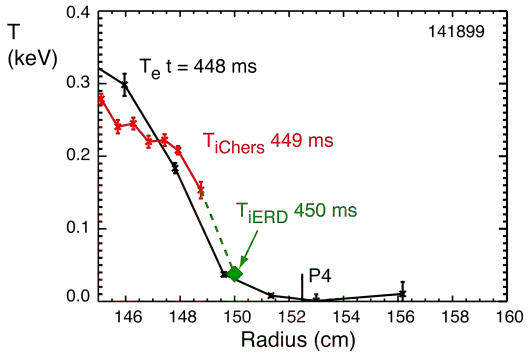

Figure 8. Edge rotation diagnostic measurement of the toroidal T_i (CIII) at 0.450 sec. and T_i Chers measurement T_i (CVI) at 0.449 sec compared to T_e at 0.448 sec. The vertical line is the extrapolated probe 4 position at the mid-plane.

For the IV characteristics in Fig. 6 and taking probe 2 to be the no RF case and probe 4 as the RF case, we have $V_{fl0} = V_{flP2} = 4$ V, and $V_{flRF0} = V_{flP4} = -20$ V as well as $T_e = 13.5$ eV and $I_{sat} = 15$ mA. Using Eqs. 10 and 11 with the assumption at first that $T_i = T_e$, gives

$\gamma_{P2} = 7.12$ $\gamma_{P4} = 14.43$

With probe dimensions of 2 mm x 7 mm [16], we obtain using Eq. 6

$q_{P2} = 0.103$ MW/m^2 $q_{P4} = 0.209$ MW/m^2

Thus, the applied RF power for the case of Section 2 is predicted to double the heat flux to the probe (and tiles) at the probe location at Bay B (Figs. 1 and 2).

A measurement of the ion temperature made with the edge rotation diagnostic (ERD) [31, 32] is shown in Fig. 8 for t = 0.450 sec for shot 141899. This temperature is for carbon (CIII) in the edge of the plasma and approximately equals T_e at R = 150 cm. A T_i measurement at the P4

position, as extrapolated to the mid-plane along a field line, is not available, but the assumption above that $T_i = T_e$ above would appear to be not unreasonable. However, T_e and T_i are expected to be decoupled in the SOL, and, to indicate the dependence of heat flux values on T_i/T_e, we consider the γ values at $T_i/T_e = 2$:

$$\gamma_{P2} = 9.42 \qquad \gamma_{P4} = 16.73,$$

and q increases to

$$q_{P2} = 0.136 \text{ MW/m}^2 \qquad q_{P4} = 0.242 \text{ MW/m}^2.$$

The background flux increases by ~ 30% and the increase with RF remains at ~ 0.1 MW/m^2.

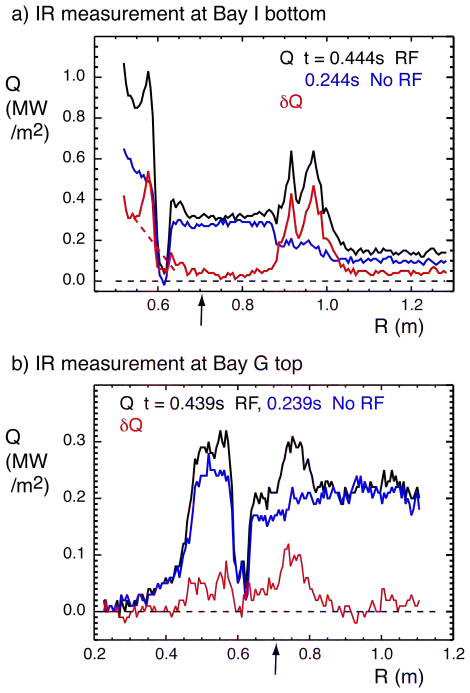

Figure 9. IR power deposition measurements for (a) Bay I bottom and (b) Bay G top (see Fig. 1). The radial location of probe 4 is indicated by arrows.

IR camera measurements are not available at the probe location (Bay B), but it is of interest to compare the probe heat flux calculations above to projections based on IR camera heat flux measurements at Bay I bottom and Bay G top (see Fig. 1) [12]. Both IR camera measurements, taken at times just prior to the time of the probe data, are shown in Fig. 9 for shot 141899; the blue curves indicate heat flux profiles with no applied RF power, black curves indicate profiles with RF power, and the red curves indicating the difference δQ. The dip in heat flux around R = 0.6 m is due to the vessel gap. For the Bay I measurement (Fig. 9a), the first (outermost) pass of the spiral across Bay I occurs between R = 0.9 – 1.0 m (the apparent two-peak structure is due to a 'notch' in the heat flux caused by tile structure). The spiral makes a second pass across Bay I just inboard of the vessel gap, around R = 0.59 m. The probes are located just outside the vessel gap (gap center at R ~ 0.6 m) with the probe 4 radial position indicated by an arrow. Around this probe radial position, the background heat flux at Bay I is roughly 0.3 MW/m^2, which is roughly twice the values for q_{P2} computed above. To get a sense for the heat flux underneath the spiral, we look to the second spiral pass. At this position, close to the outer vessel strike radius, there are two contributions to the RF-produced heat flux δQ: the direct loss of RF power in the SOL, and the plasma exhaust of RF heat coupled to the core. It is difficult to disentangle the two effects, especially as heat flux measurements are not available at smaller major radii for this shot due to hardware issues. The dashed line in Fig. 9a indicates a rough guess for the RF-produced increment in plasma exhaust; the increment in δQ above this dashed line then indicates the heat flux for the second spiral pass at Bay I, about 0.3 MW/m^2. This is about three times greater than the increment $q_{P4} - q_{P2}$ computed above; however, this increment is observed to decrease as the second pass is moved to the region outside the gap by decreasing the magnetic field pitch in the SOL [33]. Lastly, we consider the IR measurements at Bay G top, where the first pass is located outboard of the vessel gap at a major radius close the probe radii and exhibits a background of ~ 0.2 MW/m^2 and an increment due to the RF of ~ 0.1 MW/m^2. These values are closer to those calculated from the IV characteristics. It is apparent that precise quantitative comparisons are not

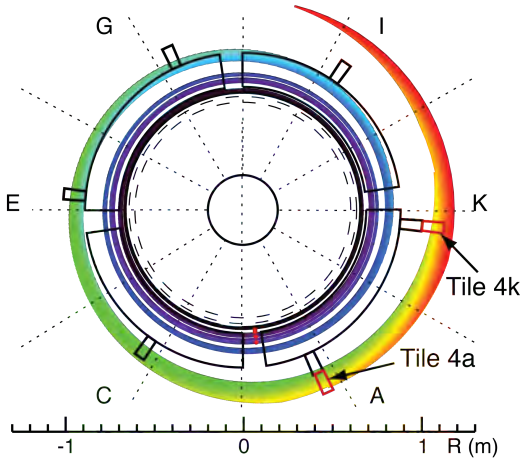

Figure 10. Calculated spiral location on lower divertor for field lines passing in front of the HHFW antenna at t = 350 ms for shot 141836. Color signifies the radial location of the line in the SOL: red is near the antenna and black is near the LCFS. Plasma conditions are B_T = 5.5 kG, I_p = 0.65 MA (magnetic pitch in the SOL ~ 27°), P_{RF} = 1.1 MW, P_{NB} = 0, and helium.

yet possible due primarily to physical separation of the measurement locations and the strong variation in spiral intensity long the length of the spiral (as described in [33]). Qualitatively, though, these IR measurements indicate that the heat flux values calculated from the IV characteristics are within a factor of two for the background, and thus a substantial part of the heat flux increment with RF is due to RF rectification as presented here. Diagnostic improvements to be found on NSTX-Upgrade will allow for more rigorous comparison and will be discussed in Section 5.

4. Probe characteristics for the P_{RF} only case

Without neutral beam injection and only RF power applied, the turbulence in the plasma edge is reduced substantially and IV characteristics with reduced fluctuation levels in the probe current are obtained. Here we consider probe characteristics for shot 141836 with P_{RF} = 1.1 MW, B_T = 5.5 kG, I_p = 0.65 MA, and helium. The SPIRAL code is again used to compute the location of the field line strike points on the lower divertor for lines passing in front of the antenna as shown in Fig. 10. At this lower pitch relative to the case of Fig. 2, the spiral is rotated clockwise so that the second pass of the spiral no longer intercepts the probes at Bay B and the first pass now falls on tiles 4k and 4a outboard of tiles 3i and 3k. For this condition the spiral now intercepts probe 1 and misses probe 3 as indicated by the floating potential measurements in Fig. 11. Again the negative shift of the floating potential with RF applied indicates RF rectification is likely present. Note that the floating potential for P1 reverses sign before the end of the RF power pulse as caused by the outer vessel strike radius (OVSR) passing over the probe [34, 16]. We will examine the IV characteristics at t ~ 0.362 sec where the OVSR is sufficiently far from the probe so as to not affect the floating potential.

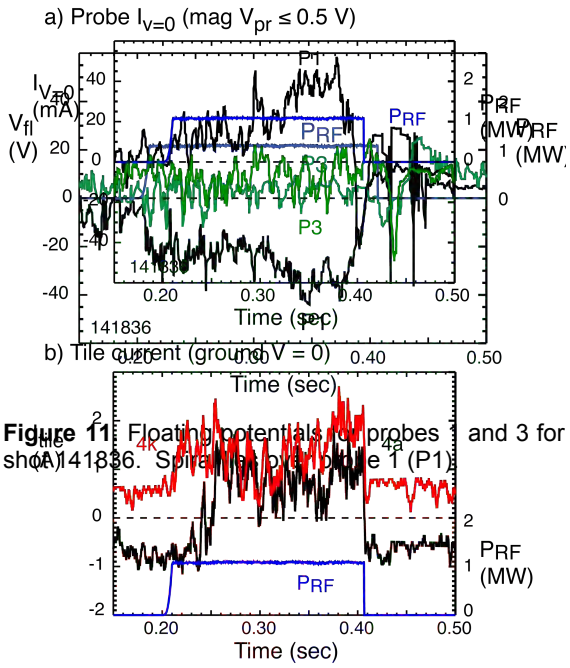

Figure 11. Floating potentials for probes 1 and 3 for shot 141836. Spiral intersects probe 1 (P1).

The currents to probes while at ground potential (V_{pr} =0) and the currents for tiles 4k and 4a are given in Fig. 12 versus time. $I_{v=0}$ for P1 responds to the applied RF pulse as did P4 in Fig. 4, and tiles 4k and 4a now respond to the RF pulse as anticipated from Fig. 10, which places the spiral over these tiles. Note that the plasma is gradually moving outward for this case as evidenced by the probe 1 V_{fl} and $I_{V=0}$ going through zero at t = 0.397 sec in Fig. 11 and Fig. 12a as the outer vessel strike radius (OVSR) passes over probe 1 [34].

The IV characteristics for probe 1 and probe 3, averaged over six consecutive 1 ms voltage sweeps starting at 0.362 sec, are shown in Fig. 13. The

Figure 12. (a) I_{pr} for probes 1 and 3 at V_{pr} = 0 (vessel potential) and (b) tile 4a and 4k currents. The probe and tiles under the spiral show significant current away from them (electron current collection) during RF heating.

characteristics exhibit much smaller current fluctuations than those of Fig. 6, and the exponential character of the probe 3 curve is much better defined. The exponential fits to the characteristics in the vicinity of the floating potentials with the same I_{sat} and T_e but with different floating potentials are quite good. We apply Eq. 5 to get an estimate of the RF voltage at the sheath for probe 1. From Fig. 11, $V_{fl} - V_{flRF} = V_{flP3} - V_{flP1} = 5.5$ V + 28 V = 33.5 V. Then, with $T_e = 34$ eV, the value of V_{RF} is 75.7 V. The common T_e in this case is 34 eV, which is considerably higher than that for Fig. 6 for the RF + NBI case. However, this value is in relatively good agreement with Thomson scattering measurements at the midplane (Fig. 14), which are also much larger than the values in Fig. 7 at the indicated radial midplane probe locations. Note that the probe locations mapped to the mid-plane are very close to the LCFS as suggested in Figs. 11 and 12a [34].

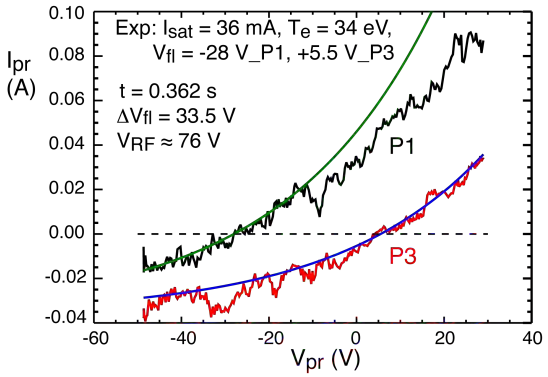

Figure 13. Probe IV characteristics for probes 1 and 3 averaged over 6 consecutive voltage sweeps starting at 0.362 sec. Exponential fits for probes 1 and 3 have the same I_{sat} and T_e, but different V_{fl} values.

The outward movement of the OVSR complicates the comparison of the heat fluxes to the probe with IR camera measurements. However, it is worth making the comparison to assure that the calculated fluxes for the probe are still in approximate range of the IR camera measurements. Assuming the ion charge Z the helium case, we modify the term (1 + ⇒ (Z + T_i/T_e) in Eq. 2 and 2.5 T_i/T_e ⇒ (2.5 T_i/T_e)/Z in Eq. 8 and Eq. 11 [35]. Then for exponentials of Fig. 13 with T_e = 34 eV, I_{sat} mA, V_{flP1} = -28 V, V_{flP3} = +5.5 V, and T_i = the = 2 in T_i/T_e) the = 36 T_e,

$\gamma_{P1} = 6.62$ $\gamma_{P3} = 5.20$,

$q_{P1} = 0.579$ MW/m^2 $q_{P3} = 0.454$ MW/m^2 $q_{P1} - q_{P3} = 0.125$ MW/m^2.

The value of q_{P1} should be slightly reduced by the saturation effect of the electron current by ~ 10% from the exponential at $V_{P1} = 0$ (Fig. 13, [35]).

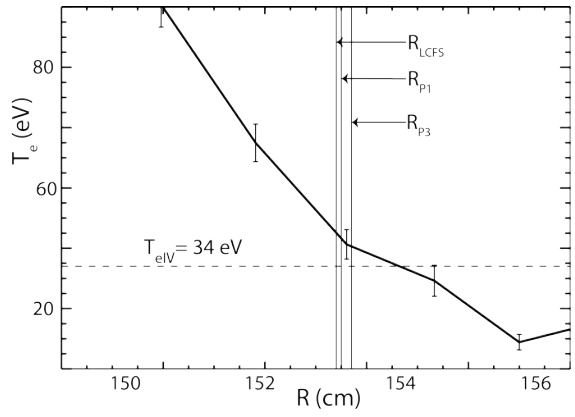

Figure 14. Probe T_e at 0.362 sec is in reasonably good agreement with Thomson scattering T_e measurements at the plasma midplane at 0.365 sec. Probes 1 and 3 map long field lines to R = 149.05 cm and 149.26 cm, and LCFS midplane radius is 149.00 cm.

The IR camera measurements taken in the vicinity of Bay I for t = 0.352 sec are shown in Fig. 15. There is no subtraction to obtain δQ due to the motion of the plasma. The heat flux profile would shift outward at the later time of the probe characteristics (0.362 – 0.368 sec) due to the plasma motion, but the radial position of the spiral passes would shift inward as one moves around the torus to the probe positions at Bay B. Figure 15 shows two peaks outside the vessel gap as has been observed for the spiral passes close to the OVSR earlier [33]. The increment in heat flux under the RF spiral in the vicinity of probe 1 is somewhere between 0.12 – 0.18 MW/m^2 depending on the exact location of the peaks

relative to the probe. However, the background calculated q_{P3} is a factor of ~ 1.8 larger than the IR camera measurement at its location. Again, these comparisons indicate that the calculated contribution of RF rectification to the heat flux to the divertor under the RF heat flux spiral could very well be within the range measured via IR thermography. However, quantitative comparisons must await HHFW operations on NSTX-U for which the probe and IR camera measurements will be co-located.

5. Conclusions and discussion

The IV characteristics for probes spaced relatively close to each other, one located under the RF heat spiral and the other located outside the spiral zone, permit comparisons without shot to shot variations. The effect of the RF on the characteristic is well represented by a negative shift in floating potential for the same exponential parameters – T_e and I_{sat}. The shift is clear for both the RF and NBI case as well as the RF-only case; however, plasma turbulence requires that several 1 ms voltage sweeps be averaged to highlight this shift. T_e values obtained from the IV characteristics compare favourably with the mid-plane Thomson scattering T_e measurements, which further supports RF rectification as the primary effect over parasitic SOL plasma heating. The negative shift in probe voltage with RF applied leads to the specification of the RF voltage across the probe sheath as a) V_{RF} = 43.7 V for P_{RF} = 1.3 MW with P_{NB} = 2 MW, and b) V_{RF} = 75.7 V for P_{RF} = 1.1 MW. Thus, the hypothesis that RF rectification is largely responsible for the response of divertor diagnostics underneath the spiral is consistent with the data, implying that heating in the SOL by the RF waves intercepting the probe may be minimal and not contributing significantly to the heat flux at the RF heat spiral.

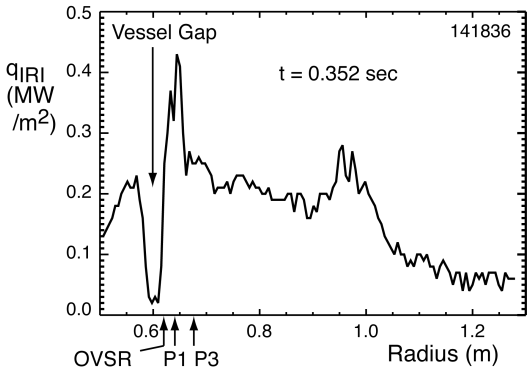

Figure 15. IR power deposition measurements for Bay I bottom (see Fig. 1). The midplane radial location of the OVSR, probe 1 and probe 3 are indicated by arrows.

We hypothesize that the heat flux increment in the spiral is also associated primarily by RF rectification in that the increase in the electron current at ground potential enhances the sheath transmission factor. This increment is ~ 0.1 MW/m^2 at the probe location as calculated for case of RF and NBI using the formula derived with an RF component to give the average sheath transmission factor γ_{RF} of Eq. 11. γ_{RF} is substantially larger than that the usual sheath transmission factor for the amplitude of V_{RF} found here. Although not measured at the probe location, IR camera measurements of the spiral heat flux at other toroidal locations show that 0.1 MW/m^2 is in the range of what would be expected for the heat flux increment at the probe location.

Based on the above results, the objective on NSTX-U will be to quantify further the RF rectification contribution to the RF heat flux spiral. First, coaxial probes located at port J, one bay clockwise from Bay I in Fig. 1, will take measurements in the brightest (hottest) part of the spiral [36]. The RF (30 MHz) component of the probe voltages should be easily measurable and will provide for direct comparison to V_{RF} measured from the floating potential shifts between adjacent probes. Ultimately, these measurements will allow for comparisons between the measured V_{RF} to that predicted from applying the AORSA code [13] to calculate E || B and V_{RF} at the probe locations, and similarly using the RF sheath boundary formalism [37]. Secondly, a

wide-view IR camera will be employed to measure the heat flux at the probe location at Bay J to compare directly with the heat fluxes calculated for the probes. This will both help quantify the RF rectification contribution to the heat flux under the spiral and help to determine the heat flux due to RF heating in the SOL prior to the waves intercepting the spiral, if any.

Acknowledgements

The authors wish to acknowledge the support of Dr. Masayuki Ono and Dr. Jonathan Menard, the NSTX team and the machine, RF, and neutral beam operations groups. This work is supported by USDOE Contract No. DE-AC02-09CH11466.

References

[1] D. W. Swain and R. H. Goulding, *Fusion Eng. Des.* **82** 603 (2007)
[2] M Ono, *Phys. Plasmas* **2**, 4075 (1995)
[3] C. E. Kessel, E. J. Synakowski, M. E. Bell, D. A. Gates, R. W. Harvey, S. M. Kaye, T. K. Mau, J. Menard, C. K. Phillips, G. Taylor, R. Wilson and the NSTX Research Team, *Nucl. Fusion* **45**, 814 (2005).
[4] D. Liu, W. W. Heidbrink, M. Podestà, R. E. Bell, E. D. Fredrickson, S. S. Medley, R. W. Harvey, and E. Ruskov, *Plasma Phys. Control. Fusion* **52**, 025006 (2010).
[5] M. Podestà, R. E. Bell, E. D. Fredrickson, N. N. Gorelenkov, B. P. LeBlanc, W. W. Heidbrink, N. A. Crocker, S. Kubota and H. Yuh, *Phys. Plasmas* **17**, 122501 (2010).
[6] E. D. Fredrickson1, G. Taylor, N. Bertelli, D. S. Darrow, N. Gorelenkov, G. Kramer, D. Liu, N. A. Crocker, S. Kubota and R. White, *Nucl. Fusion* **55** 013012 (2015).
[7] M. Ono, S. M. Kaye, Y.-K. M. Peng, G. Barnes, W. Blanchard, M. D. Carter, J. Chrzanowski, L. Dudek, R. Ewig, D. Gates, R. E. Hatcher, T. Jarboe, S. C. Jardin, D. Johnson, R. Kaita, M. Kalish, C.E. Kessel, H.W. Kugel, R. Maingi, R. Majeski, J. Manickam, B. McCormack, J. Menard, D. Mueller, B. A. Nelson, B. E. Nelson, C. Neumeyer, G. Oliaro, F. Paoletti, R. Parsells, E. Perry, N. Pomphrey, S. Ramakrishnan, R. Raman, G. Rewoldt, J. Robinson, A. L. Roquemore, P. Ryan, S. Sabbagh, D. Swain, E. J. Synakowski, M. Viola, M. Williams, J. R. Wilson and NSTX Team, *Nucl. Fusion* **40**, 557 (2000).
[8] J. Hosea, R. E. Bell, B. P. LeBlanc, C. K. Phillips, G. Taylor, E. Valeo, J. R. Wilson, E. F. Jaeger, P. M. Ryan, J. Wilgen, H. Yuh, F. Levinton, S. Sabbagh, K. Tritz, J. Parker, P. T. Bonoli, R. Harvey and the NSTX Team, *Phys. Plasmas* **15**, 056104 (2008).
[9] J. C. Hosea, R. E. Bell, E. Feibush, R. W. Harvey, E. F. Jaeger, B. P. LeBlanc, R. Maingi, C. K. Phillips, L. Roquemore, P. M. Ryan, G. Taylor, K. Tritz, E. J. Valeo, J. Wilgen, J. R. Wilson, and the NSTX Team, *AIP Conf. Proc.* 1187, 105 (2009).
[10] C. K. Phillips, R. E. Bell, L. A. Berry, P. T. Bonoli, R. W. Harvey, J. C. Hosea, E. F. Jaeger, B. P. LeBlanc, P. M. Ryan, G. Taylor, E. J. Valeo, J. B. Wilgen, J. R. Wilson, J. C. Wright, H. Yuh and the NSTX Team, *Nucl. Fusion* **49**, 075015 (2009).
[11] G. Taylor, R. E. Bell, J. C. Hosea, B. P. LeBlanc, C. K. Phillips, M. Podesta, E. J. Valeo, J. R. Wilson, J-W. Ahn, G. Chen, D. L. Green, E. F. Jaeger, R. Maingi, P. M. Ryan, J. B. Wilgen, W. W. Heidbrink, D. Liu, P. T. Bonoli, T. Brecht, M. Choi and R. W. Harvey, *Phys. Plasmas* **17**, 056114 (2010).
[12] D. Mastrovito, R. Maingi, H. W. Kugel, and A. L. Roquemore, *Rev. Sci. Instrum.* **74,** 5090 (2003).

[13] N. Bertelli, E. F. Jaeger, J. C. Hosea, C. K. Phillips, L. Berry, S.P. Gerhardt, D. Green, B. LeBlanc, R. J. Perkins, P. M. Ryan, G. Taylor, E. J. Valeo, and J. R. Wilson, *Nuclear Fusion* **54**, 083004 (2014).
[14] R. J. Perkins, J. C. Hosea, G. J. Kramer, J.-W. Ahn, R. E. Bell, A. Diallo, S. Gerhardt, T. K. Gray, D. L. Green, E. F. Jaeger, M. A. Jaworski, B. P. LeBlanc, A. McLean, R. Maingi, C. K. Phillips, L. Roquemore, P. M. Ryan, S. Sabbagh, G. Taylor, and J. R. Wilson, *Phys. Rev. Lett.* **109**, 045001 (2012).
[15] G. J. Kramer, R. V. Budny, A. Bortolon, E. D. Fredrickson, G. Y. Fu, W. W. Heidbrink, R. Nazikian, E. Valeo, and M. A. Van Zeeland, *Plasma Phys. Contr. Fusion* **55**, 025013 (2013).
[16] J. Kallman, M. A. Jaworski, R. Kaita, H. Kugel, and T. K. Gray, *Rev. Sci. Instrum.* **81**, 10E117 (2010).
[17] M. A. Jaworski, J. Kallman, R. Kaita, H. Kugel, B. LeBlanc, R. Marsala, and D. N. Ruzic, *Rev. Sci. Instrum.* **81**, 10E130 (2010).
[18] S. P. Gerhardt, E. Fredrickson, L. Guttadora, R. Kaita, H. Kugel, J. Menard, and H. Takahashi, *Rev. Sci. Instrum.* **82**, 103502 (2011).
[19] A. Boschi and F. Magistrelli, *Il Nuovo Cimento* **29**, 487 (1963).
[20] H. S. Butler and G. S. Kino, *Phys. Fluids* **6**, 1346 (1963).
[21] S. J. Wukitch, M. L. Garrett, R. Ochoukov, J. L. Terry, A. Hubbard, B. Labombard, C. Lau, Y. Lin, B. Lipschultz, D. Miller, M. L. Reinke, D. Whyte, and the Alcator C-Mod Team, *Phys. Plasmas* **20**, 056117 (2013).
[22] Vl. V. Bobkov, F. Braun, R. Dux, A. Herrmann, L. Giannone, A. Kallenbach, A. Krivska, H.W. Müller, R. Neu, J.-M. Noterdaeme, T. Pütterich, V. Rohde, J. Schweinzer, A. Sips, I. Zammuto, and the ASDEX Upgrade Team, *Nucl. Fusion* **50**, 035004 (2010).
[23] C. C. Klepper, P. Jacquet, V. Bobkov, L. Colas, T. M. Biewer, D. Borodin, A. Czarnecka, C. Giroud, E. Lerche, V. Martin, M.-L. Mayoral, F. Rimini, G. Sergienko, D. Van Eester, JET EFDA contributors, *J. Nucl. Mater.* **438**, S594 (2013).
[24] L. Colasa, D. Milanesio, E. Faudot, M. Goniche, and A. Loarte, *J. Nucl. Mater.* **309-391**, 959 (2009).
[25] P. Jacquet, F. Marcotte, L. Colas, G. Arnoux, V. Bobkov, Y. Corre, S. Devaux, J.-L. Gardarein, E. Gauthier, M. Graham, E. Lerche, M.-L. Mayoral, I. Monakhov, F. Rimini, A. Sirinelli, D. Van Eester, and JET EFDA contributors, *J. Nucl. Mater.* **438**, S379 (2013).
[26] J. R. Myra, D. A. D'Ippolito, and M. Bures, *Phys. Plasmas* **1**, 2890 (1994).
[27] C. C. Petty, F. W. Baity, J. S. deGrassie, C. B. Forest, T. C. Luce, T. K. Mau, M. Murakami, R. I. Pinsker, P. A. Politzer, M. Porkolab and R. Prater, *Nucl. Fusion* **39**, 1421 (1999).
[28] J. R. Sanmartin, *Phys. Fluids* **13**, 1 (1970).
[29] P.C. Stangby, "The Plasma Boundary of Magnetic Fusion Devices", *Plasma Physics Series* (published by Taylor and Francis Group 2000).
[30] M. Abramowitz and I. A. Stegun, "Handbook of Mathematical Functions", *National Bureau of Standards Applied Mathematics Series 55* (1964).
[31] T. M. Biewer, R. E. Bell, R. Feder, D. W. Johnson, and R. W. Palladino, *Rev. Sci. Instrum.* **75**, 650 (2004).
[32] T. M. Biewer, R. E. Bell, S. J. Diem, C. K. Phillips, J. R. Wilson, and P. M. Ryan, *Phys. Plasmas* **12**, 056108 (2005).

[33] R. J. Perkins, J.-W. Ahn, R. E. Bell, A. Diallo, S. Gerhardt, T. K. Gray, D. L. Green, E. F. Jaeger, J. C. Hosea, M. A. Jaworski, B. P. LeBlanc, G. J. Kramer, A. McLean, R. Maingi, C. K. Phillips, M. Podestà, L. Roquemore, P. M. Ryan, S. Sabbagh, F. Scotti, G. Taylor and J. R. Wilson, *Nucl. Fusion* **53,** 083025 (2013).

[34] J. C. Hosea, R. Perkins, M. A. Jaworski, G. J. Kramer, J.-W. Ahn, N. Bertelli, S. Gerhardt, T. K. Gray, B. P. LeBlanc, R. Maingi, C. K. Phillips, L. Roquemore, P. M. Ryan, S. Sabbagh, G. Taylor, K. Tritz, J. R. Wilson and the NSTX Team, *AIP Conf. Proc.* **1580**, 251 (2014).

[35] D. Brunner and B. LaBombard, *Rev. Sci. Instrum.* **83**, 033501 (2012).

[36] R. J. Perkins, J-W. Ahn, R. E. Bell, N. Bertelli, A. Diallo, S. Gerhardt, T. K. Gray, D. L. Green, E. F. Jaeger, J. C. Hosea, M. A. Jaworski, B. P. LeBlanc, G. J. Kramer, A. McLean, R. Maingi, C. K. Phillips, M. Podestà, L. Roquemore, P. M. Ryan, S. Sabbagh, F. Scotti, G. Taylor and J. R. Wilson, *AIP Conf. Proc.* **1580**, 81 (2014).

[37] D. A. D'Ippolito, J. R. Myra, R. Ochoukov, and D. G. Whyte, *Plasma Phys. Contr. Fusion* **55**, 085001 (2013).

Princeton Plasma Physics Laboratory
Office of Reports and Publications

Managed by
Princeton University

under contract with the
U.S. Department of Energy
(DE-AC02-09CH11466)

P.O. Box 451, Princeton, NJ 08543
Phone: 609-243-2245
Fax: 609-243-2751

E-mail: publications@pppl.gov
Website: http://www.pppl.gov